JACS
JOURNAL OF THE AMERICAN CHEMICAL SOCIETY
Article
Cite This: J. Am. Chem. Soc. 2018, 140, 1549−1556
pubs.acs.org/JACS

From Alloy-Like to Cascade Blended Structure: Designing High-Performance All-Small-Molecule Ternary Solar Cells

Zhen Wang,[†,‡,§] Xiangwei Zhu,[†] Jianqi Zhang,[†] Kun Lu,[*,†] Jin Fang,[†] Yajie Zhang,[†] Zaiyu Wang,[∥] Lingyun Zhu,[*,†] Wei Ma,[*,∥] Zhigang Shuai,[‡] and Zhixiang Wei[*,†,§]

[†]CAS Key Laboratory of Nanosystem and Hierarchical Fabrication, CAS Center for Excellence in Nanoscience, National Center for Nanoscience and Technology, Beijing 100190, PR China

[‡]MOE Key Laboratory of Organic Optoelectronics and Molecular Engineering, Department of Chemistry, Tsinghua University, Beijing 100084, PR China

[§]University of Chinese Academy of Sciences, Beijing 100049, PR China

[∥]State Key Laboratory for Mechanical Behavior of Materials, Xi'an Jiaotong University, Xi'an 710049, PR China

Supporting Information

ABSTRACT: Ternary blending strategy has been used to design and fabricate efficient organic solar cells by enhancing the short-circuit current density and the fill factor. In this manuscript, we report all-small-molecule ternary solar cells consisting of two compatible small molecules DR3TBDTT (**M1**) and DR3TBDTT-E (**M2**) as donors and $PC_{71}BM$ as acceptor. A transformation from an alloy-like model to a cascade model are first realized by designing a novel molecule **M2**. It is observed that after thermal and solvent vapor annealing **M2** shifts from the mixed region to donor−acceptor (D−A) interfaces which ameliorates the charge transfer and recombination processes. The optimal ternary solar cells with 10% **M2** exhibited a power conversion efficiency of 8.48% in the alloy-like model and 10.26% in the cascade model. The proposed working mechanisms are fully characterized and further supported by the density functional theory and atomistic molecular dynamics simulations. This provides an important strategy to design high-performance ternary solar cells which contains one molecule not only is compatible with the main donor molecule but also performs a preference to appear at the D−A interfaces hence builds cascade energy levels.

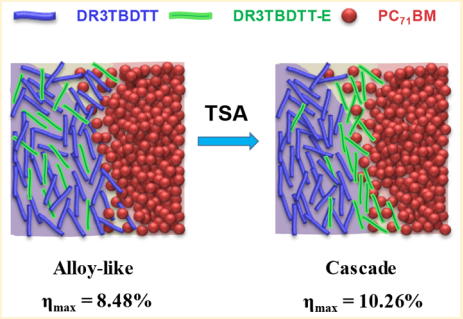

INTRODUCTION

Organic solar cells (OSCs) have been extensively investigated because of several advantages, including low cost, light weight, easy processing, and flexibility.[1−3] Designing novel molecules and tuning bulk heterojunctions (BHJs) of active layers have contributed to the improvement of the performance of OSCs. The power conversion efficiencies (PCEs) of OSCs for polymers and small molecules have respectively exceeded over 13 and 11% by designing appropriate molecules and optimizing the morphological characteristics of BHJs.[4,5] To overcome the light harvest shortage of solar light, researchers fabricated ternary blend solar cells consisting of two electron-donating materials with different structures and one electron-withdrawing acceptor or one donor and two acceptors.[6−8] Ternary blends have been demonstrated as efficient strategy to increase the light-harvesting efficiency and tune the morphological characteristics of BHJs.

With the development of ternary OSCs, different models and mechanisms have been proposed to guide the design of ternary blends. You et al. reported a parallel-like model for ternary OSCs by applying two conjugated polymers as donors, which form bicontinuous interpenetrating networks with a fullerene phase.[9] Thompson et al. proposed an alloy model for OSCs by studying the origin of the tunable open-circuit voltage (V_{OC}) of a series of ternary BHJ solar cells.[10−12] In the alloy model, two donor molecules with a small Flory−Huggins interaction parameter are properly mixed, and they consequently form alloy-like domains, which exhibit the proportionally highest occupied molecular orbital (HOMO) level; thus, ternary solar cells yield a tunable V_{OC} as the ratio of these donors varies.[13] Yang et al. suggested that two donors with similar chemical and physical properties should be selected because unfavorable interactions among three components may function as morphological traps and recombination centers.[14] Our group investigated the synergistic effect of a polymer and a small molecule with a similar chemical backbone in ternary blends and revealed that an optimal alloy-like structure of the small molecule and the polymer can induce the crystallinity of polymer domains and result in the formation of favorable nanostructures, which can simultaneously increase the short-circuit current density (J_{SC}) and fill factor (FF).[15,16] The third component can generally extend the absorption of the solar

Received: December 10, 2017
Published: January 10, 2018

DOI: 10.1021/jacs.7b13054
J. Am. Chem. Soc. 2018, 140, 1549−1556

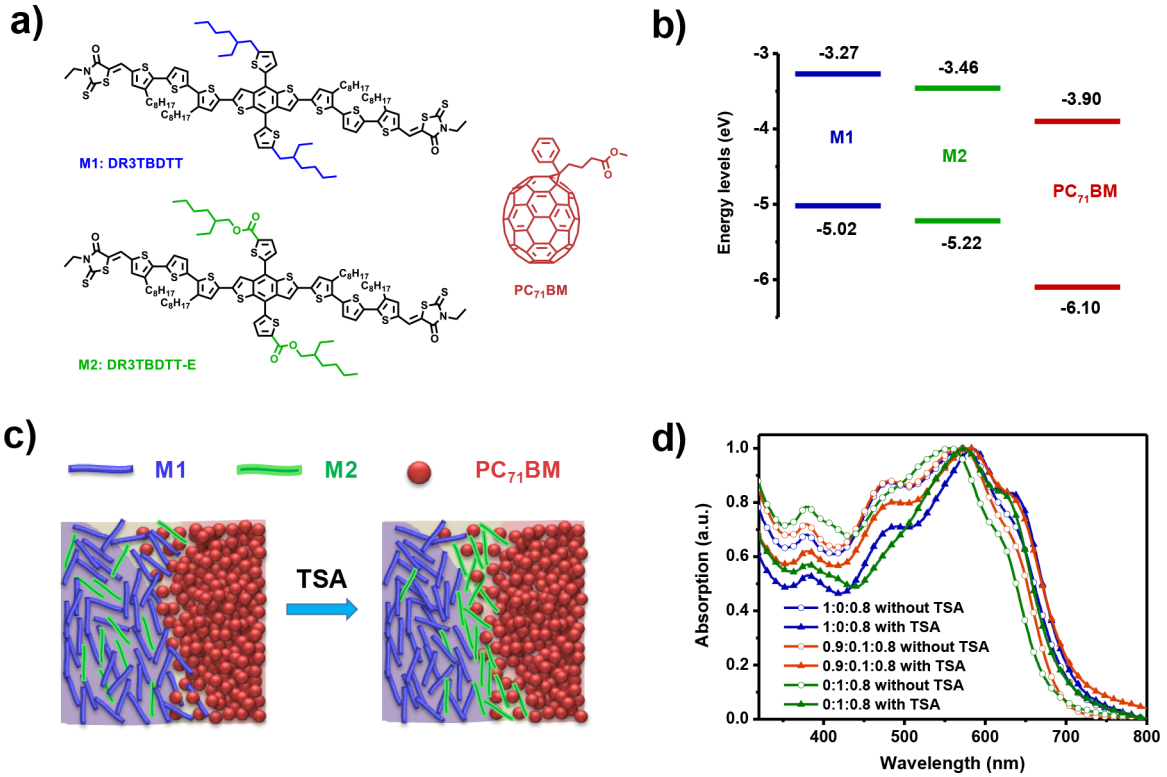

Figure 1. (a) Chemical structures of DR3TBDTT (**M1**), DR3TBDTT-E (**M2**), and $PC_{71}BM$. (b) Energy levels of **M1**, **M2**, and $PC_{71}BM$. (c) Diagrammatic sketch of the phase transformation before and after TSA. (d) UV−vis absorption spectra of the active layers of selected systems with and without TSA.

spectrum or optimize the morphological characteristics of OSCs.[6−8,17,18]

In addition to molecule and BHJ mesophase optimization, exciton separation and charge transport for BHJ organic solar cells are facilitated by donor−acceptor (D−A) interfaces.[19−21] McGehee et al. proposed that mixed regions exist at D−A interfaces in polymer:fullerene binary solar cells, and low charge carrier recombination and high internal quantum efficiency can be accomplished by carefully modifying the mixed regions.[19,20] A ternary strategy, especially for three components with cascade energy levels, provides a potential mechanism to optimize D−A interfaces.[22,23] The cascade energy levels of ternary blends are beneficial to charge transfer, while charge recombination is minimized.[24−29] Ameri et al. presented strategies based on a cascade model to decrease charge carrier recombination at D−A interfaces by employing third compounds.[30,31] In a PTB7:sensitizer:fullerene ternary system, an effective charge transfer occurs from a disordered host system to a highly ordered sensitizer, which effectively avoids traps of host matrices and features an almost ideal recombination behavior.[31] Thus, designing a ternary OSC system containing one molecule not only exhibits compatibility with the main donor molecule but also preferably appears at D−A interfaces and hence builds cascade energy levels will be much likely to enhance the performance of OSCs.

Herein, strengthening the interaction between the third component and 6,6-phenyl-C_{71}-butyric acid methyl ester ($PC_{71}BM$) is proposed to reach the aforementioned goal in a $PC_{71}BM$-containing ternary system, which can be realized by introducing an ester functional group to electron-donating molecules. In accordance with this guideline, all-small-molecule ternary OSCs consisting of two compatible small molecules, namely, DR3TBDTT (**M1**)[32] and DR3TBDTT-E (**M2**), as donors and $PC_{71}BM$ as an acceptor are designed and fabricated. **M2** is a key novel small molecule that contains thiophene-substituted benzo[1,2-*b*:4,5-*b*′]dithiophene (BDT) with ester-anchored alkyl side chains as a donor moiety and 3-ethylrhodanine (RHD) as acceptors connected with terthiophene π-conjugated bridges (Scheme S1). The chemical structures of **M1**, **M2**, and $PC_{71}BM$ are shown in Figure 1a. The obtained ternary OSCs without post-treatment yield a PCE of 8.48% with V_{OC} of 0.931 V, J_{SC} of 12.82 mA cm^{-2}, and FF of 71.1%. After these OSCs are thermally annealed at 70 °C for 5 min and then subjected to solvent vapor annealing in chloroform vapor at room temperature for 1 min (TSA), PCE is enhanced to 10.26% with a V_{OC} of 0.896 V, J_{SC} of 14.97 mA cm^{-2}, and FF of 76.5%. The enhancement after TSA is attributed to the transformation of an alloy-like model to a cascade model accompanied by the transformation from dynamic balance to thermodynamic balance. These processes occur because **M2** shifts from the mixed region to the D−A interface, which ameliorates the charge transfer and the recombination processes.

RESULTS AND DISCUSSION

Molecular Energy Levels and UV−Vis Absorption Spectra. The electrochemical HOMO/lowest unoccupied molecular orbital (LUMO) levels of **M1** and **M2** are approximately −5.02/−3.27 eV and −5.22/−3.36 eV, respectively. The cyclic voltammogram of the **M2** thin film is shown in Figure S1. The optical and electrochemical data of these two small molecules are listed in Table S1. The energy levels for **M2** are lowered by introducing ester functions to side chains, and energy cascades are formed in the LUMO and HOMO levels of

DOI: 10.1021/jacs.7b13054
J. Am. Chem. Soc. 2018, 140, 1549−1556

Table 1. Summary of the Photovoltaic Parameters of Solar Cells with Different M1:M2 Ratios without Post Treatment

M1:**M2**:$PC_{71}BM$	V_{OC} (V)	J_{SC} (mA/cm^2)	FF (%)	PCE_{ave} (%)	PCE_{max} (%)
1:0:0.8	0.906 ± 0.002	12.73 ± 0.37	65.8 ± 1.4	7.50 ± 0.09	7.59
0.9:0.1:0.8	0.931 ± 0.002	12.82 ± 0.25	71.1 ± 0.4	8.30 ± 0.16	8.48
0.8:0.2:0.8	0.936 ± 0.001	12.00 ± 0.05	66.5 ± 0.8	7.43 ± 0.06	7.47
0.6:0.4:0.8	0.943 ± 0.001	11.87 ± 0.04	61.5 ± 0.7	6.82 ± 0.07	6.88
0.4:0.6:0.8	0.957 ± 0.004	11.21 ± 0.14	59.2 ± 0.8	6.29 ± 0.05	6.35
0.2:0.8:0.8	0.970 ± 0.006	10.32 ± 0.03	55.9 ± 0.6	5.54 ± 0.08	5.60
0:1:0.8	1.002 ± 0.003	8.37 ± 0.18	48.1 ± 1.5	3.89 ± 0.11	4.04

Table 2. Summary of the Photovoltaic Parameters of Solar Cells with Different M1:M2 Ratios with TSA

M1:**M2**:$PC_{71}BM$	V_{OC} (V)	J_{SC} (mA/cm^2)	FF (%)	PCE_{ave} (%)	PCE_{max} (%)
1:0:0.8	0.880 ± 0.004	13.52 ± 0.06	74.9 ± 0.3	8.83 ± 0.06	8.90
0.9:0.1:0.8	0.896 ± 0.006	14.97 ± 0.20	76.5 ± 1.2	10.02 ± 0.12	10.26
0.8:0.2:0.8	0.901 ± 0.003	12.67 ± 0.10	74.7 ± 0.5	8.44 ± 0.07	8.52
0.6:0.4:0.8	0.895 ± 0.002	12.56 ± 0.14	61.5 ± 0.3	6.89 ± 0.03	6.92
0.4:0.6:0.8	0.902 ± 0.003	12.38 ± 0.08	58.4 ± 0.5	6.51 ± 0.01	6.52
0.2:0.8:0.8	0.920 ± 0.002	11.24 ± 0.09	54.7 ± 1.4	5.47 ± 0.19	5.66
0:1:0.8	0.944 ± 0.005	10.85 ± 0.27	68.2 ± 1.1	6.94 ± 0.04	6.99

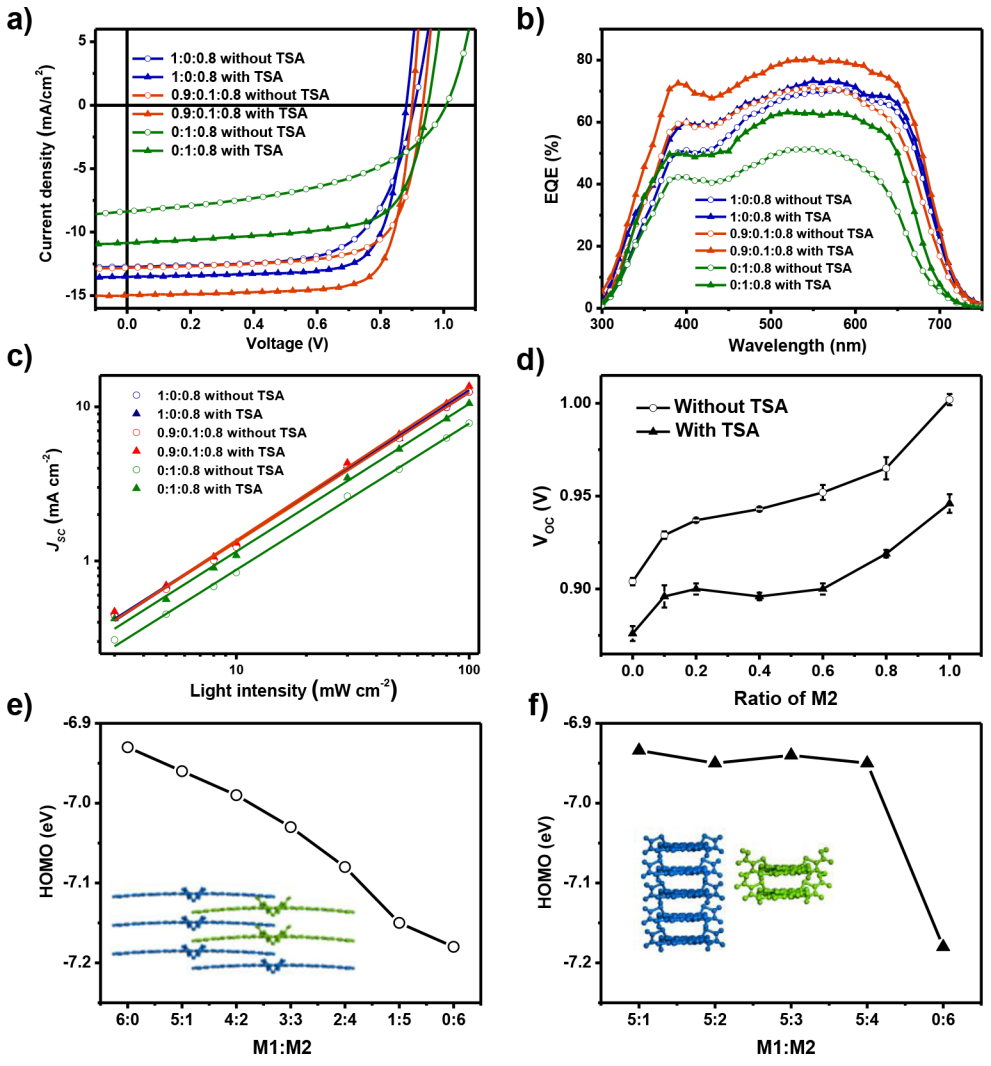

Figure 2. (a) J–V curves of OSCs with **M1**:**M2**:$PC_{71}BM$ ratios of 1:0:0.8, 0.9:0.1:0.8, and 0:1:0.8 with and without TSA. (b) EQE curves of the OSCs that correspond to the devices in panel a. (c) Dependence of J_{SC} on the light intensity for the OSCs that correspond to the devices in panel a. (d) V_{OC}'s of OSCs with different **M1**:**M2** weight ratios with and without TSA. (e–f) Calculated HOMO as a function of the **M1**:**M2** ratios of complexes with alloy-like (e) and cascade (f) packing patterns.

DOI: 10.1021/jacs.7b13054
J. Am. Chem. Soc. 2018, 140, 1549–1556

the three compounds (Figure 1b). The UV−vis absorption spectra of the ternary and binary systems were examined (see Figure 1d) to determine the photochemical effect of doping **M2** into **M1**:$PC_{71}BM$ blends. The **M1**:$PC_{71}BM$ binary films exhibit more red-shifted absorption edge than the **M2**:$PC_{71}BM$ films before and after TSA. However, the **M2**:$PC_{71}BM$ films showed stronger absorption intensities in the range of 300−550 nm. At the optimized ratio of **M1**:**M2** (0.9:0.1), the absorption intensities are enhanced in the range of 300−550 nm compared with the **M1**:$PC_{71}BM$ films. The absorption band edge is comparable with the **M1**:$PC_{71}BM$ films. Thus, the inducement of **M2** can enhance the absorption ability in the range of 300−550 nm.

Photovoltaic Properties. Binary and ternary solar cells were then fabricated with conventional device structures of indium tin oxide (ITO)/PEDOT:PSS/active layer/Ca/Al. The experimental details can be referenced in the Supporting Information. The performances of the solar cells are listed in Tables 1 and 2, and the $J-V$ curves under AM 1.5 G illuminations at 100 mW cm^{-2} are shown in Figure 2a. Active layers for binary and ternary blends performed thin thicknesses of 80−90 nm. Without any post treatment, the **M1**:$PC_{71}BM$-based devices exhibit an efficiency level of 7.59% with a V_{OC} of 0.906 V, J_{SC} of 12.73 mA cm^{-2}, and FF of 65.8%, whereas the **M2**:$PC_{71}BM$-based solar cells show a lower PCE of 4.04% with a V_{OC} of 1.002 V, J_{SC} of 8.37 mA cm^{-2}, and FF of 48.1%. The ternary solar cells at the optimized ratio of **M1**:**M2** (0.9:0.1) yield an increased PCE of 8.48% with a V_{OC} of 0.931 V, J_{SC} of 12.82 mA cm^{-2}, and FF of 71.1%. After carefully controlled thermal annealing at 70 °C for 5 min and solvent vapor annealing in chloroform vapor at room temperature for 60 s, the performances of the binary and ternary solar cells with **M1**:**M2**:$PC_{71}BM$ ratios of 0.9:0.1:0.8 and 0.8:0.2:0.8 are significantly enhanced. The **M1**:$PC_{71}BM$-based devices exhibit an PCE of 8.90% with a V_{OC} of 0.880 V, J_{SC} of 13.52 mA cm^{-2}, and FF of 74.9%, whereas **M2**:$PC_{71}BM$-based solar cells perform a lower PCE of 6.99% with a V_{OC} of 0.944 V, J_{SC} of 10.85 mA cm^{-2}, and FF of 68.2%. A remarkable PCE of 10.26% with a V_{OC} of 0.896 V, J_{SC} of 14.97 mA cm^{-2}, and FF of 76.5% is attained by the optimal ternary OSCs. The $J-V$ curves show that the inducement of 10% (weight ratio) of the **M2** to **M1**:$PC_{71}BM$ system does increase the J_{SC} and FF of the devices. The external quantum efficiency (EQE) results (Figure 2b) are consistent with the J_{SC} values of the corresponding OSCs. The deviations between the integral current densities and J_{SC} read from the $J-V$ measurements are under 3%, which indicate a suitable consistency of the photovoltaic results. The enhanced EQE for the ternary system surely does not originate from the sum of **M1** and **M2** because it is higher than either of the two small molecules. A new photophysical mechanism should be proposed for the optimal ternary solar cells.

Bimolecular Recombination Analysis. Bimolecular recombination is studied by mapping J_{SC} as a function of the incident light intensity of the selected systems (Figure 2c). The J_{SC} follows the power−law dependence on light intensity, which can be expressed as $J_{SC} \propto P_{Light}^{\alpha}$.[33,34] In this case, P_{Light} is the light intensity, and α is the exponential factor. Weak bimolecular recombination in the device would result in a linear dependence of J_{SC} on the light intensity with α value close to 1.[35] The exponential factors for **M1**:$PC_{71}BM$-, **M1**:**M2**:$PC_{71}BM$ (0.9:0.1:0.8)-, and **M2**:$PC_{71}BM$-based solar cells before TSA are 0.964, 0.972, and 0.950, respectively, whereas those after TSA are 0.983, 0.994, and 0.958, respectively. We can conclude that the ternary blending and TSA treatment lower the bimolecular recombination in solar cells. In the optimized ternary solar cells, the lowest bimolecular recombination results in a high J_{SC} and subsequently high PCE.

Open-Circuit Voltage Evolution. The V_{OC}'s evolution with different **M1**:**M2** ratios, as well as before and after thermal and solvent vapor treatment, are investigated. The statistical summary of the change in V_{OC}'s is shown in Figure 2d. The V_{OC}'s before TSA are higher and exhibit a tendency of quasi-linear change along with the **M2** weight ratio increase in the ternary blends. The highest V_{OC} of 1.002 V is obtained by the **M2**:$PC_{71}BM$-based solar cells, which prove a deeper HOMO level of **M2**. V_{OC}'s after TSA showed a subtle varying trend. In particular, V_{OC} is approximately 0.90 V with an **M2** ratio between 10 and 60%, whereas the V_{OC}'s changed accordingly with an **M2** ratio of below 10% or above 80%. Different models for ternary blend solar cells could help us understand the subtle differences in V_{OC} changing tendencies before and after TSA. The alloy-like model can explain the tunable V_{OC}'s of ternary systems without any post treatment. The cascade model could be employed to explain the pinned V_{OC} of ternary solar cells with a **M2** ratio of 10% to 60% after TSA. With a very small amount (e.g., less than 10% weight ratio), and even after TSA, the third component will most likely be embedded in the host phases, in which case the chemical and photophysical properties of the third component maybe disregarded. By contrast, with a **M2** ratio of 10−60%, the third component is supposed to locate at the D−A interfaces and serve as a sensitizer to form a cascade energy level. When the **M2** ratio is higher than 60% and after TSA treatment, the **M1** is embedded in the **M2** host phases and acts as an alloy-like phase separation, which also shows a quasi-linear change for V_{OC}. Thus, we can assume a transformation from an alloy-like model to a cascade model (Figure 1c) occurred for the optimized ternary solar cells, especially at the **M2** ratio of 10−60%, in which **M2** shifts from the mixed region to D−A interface as a result of TSA.

Charge Transport Processes. The femtosecond transient absorption spectra (fs-TAS) measurements were performed to figure out the charge transport processes in the binary and ternary blend films. As is shown in Figure S2a−c, without TSA, the **M1**:$PC_{71}BM$-based film shows three absorption peaks of 482, 582, and 683 nm, and the **M2**:$PC_{71}BM$-based film only shows two peaks of 570 and 626 nm. As for the ternary blend film, three distinguished peaks are located, and the one of 480 nm is slightly enhanced. Therefore, the decays of the photoluminescence probed at 480 nm were measured. As can be seen in Figure S2d and Table S2, the charge carrier life times (τ_1, τ_2, and τ_3) are lengthened, and the data of films with TSA exhibits the very similar phenomenon (Figure S3 and Table S3). We conclude that there are charge transport processes from **M2** to **M1** both in the alloy-like model and the cascade model. The different is that in the cascade model excitons generated by the **M2** can split with the $PC_{71}BM$ to generate charge carriers and then transport via the **M1** and $PC_{71}BM$. In the alloy-like model, the charge separation and transport processes are likely similar as in the conventional BHJ structures, but the donor phase is **M1**:**M2** alloy.

Density Functional Theory Simulations. To enhance our understanding of the origin of V_{OC} changes in the alloy-like and cascade blending structures, density functional theory (DFT) calculations are performed using long-range corrected functional ωB97X with 6-31G (d,p) basis set. The computational details can be referenced in SI. Two different types of

DOI: 10.1021/jacs.7b13054
J. Am. Chem. Soc. 2018, 140, 1549−1556

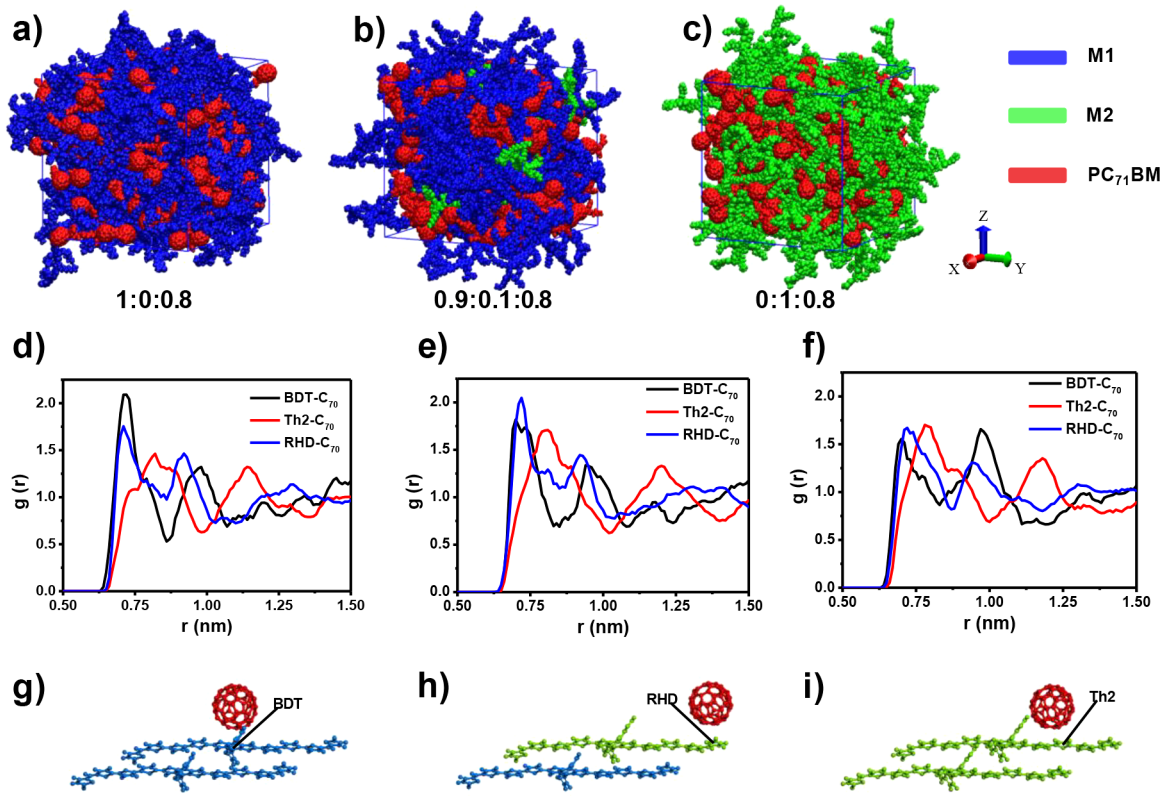

Figure 3. (a–c) Unit cell snapshots of equilibrated systems with **M1**:**M2**:$PC_{71}BM$ ratios of 1:0:0.8, 0.9:0.1:0.8, and 0:1:0.8. (d–f) Center-of-mass radial distribution functions of systems that correspond to (a–c). (g–i) Schematic of systems that correspond to (a–c), in which the side chains were excluded.

complexes are constructed to model the alloy-like and cascade packing patterns based on the optimized **M1** and **M2** monomers (see Figures S4 and S6 in SI). The **M1** and **M2** molecules in alloy-like model are combined along the stacking direction (**M1**-**M2**-**M1**...), whereas those in the cascade model form adjacent separated stacks (...**M1**-**M1**-**M1**... and ...**M2**-**M2**-**M2**...). The intermolecular distances along the stacking direction are maintained at 3.6 Å in all cases. Figure S5 shows that for the alloy-like model complexes, the HOMO orbitals are delocalized on the **M1** molecule and varied with the increase in the number of **M2** molecule. As expected, an approximately linear relationship is noted between the HOMO energy of the complexes and ratio of **M1**:**M2** (Figure 2e). This condition is consistent with the findings of Thompson et al. in the alloy-like model. However, the HOMO orbitals (Figure S7) in the cascade model complexes are localized on the **M1** molecules, and the HOMO energy is independent of the increase in the number of the **M2** molecule (Figure 2f). Thus, our calculations fully support the experimentally observed transformation from alloy-like to cascade packing in the blended structure.

Theoretical simulations are also performed to calculate the binding energies of **M1**-$PC_{71}BM$, **M2**-$PC_{71}BM$, and **M1**-**M2**. The geometries of the complex structures are optimized with DFT methods with the long-range corrected functional CAM-B3LYP and 6-31G (d,p) basis set, shown in Figure S8. Results show that the **M1**-**M2** complex has a binding energy (−10.0 kcal mol^{-1}) larger than those of other two complexes (−3.8 kcal mol^{-1} for **M1**-$PC_{71}BM$ and −5.0 kcal mol^{-1} for **M2**-$PC_{71}BM$, respectively), which indicates that these two molecules have suitable compatibility. A stronger intermolecular interaction was also observed for the **M2**-$PC_{71}BM$ complex than **M1**-$PC_{71}BM$ complex, which means a larger probability for **M2** to appear at donor−$PC_{71}BM$ interfaces. Ester side chains with withdrawing ability can also modify the energy level of **M2**, which can benefit the formation of the cascade blending structure in ternary systems.

Molecular Dynamics Simulations. To obtain insights into the molecular packing in the mixed regions in binary and optimized ternary blends, atomistic molecular dynamics (MD) simulations were performed using the GROMACS 4.6.7 software suite.[36] The computational details can be referenced in the Supporting Information, and the results are shown in Figure 3a–c. Figure 3b shows that **M2** tends to locate at the interfaces between **M1** and $PC_{71}BM$ in the mixed regions of the ternary system, which indicates that **M2** has a stronger interaction with $PC_{71}BM$ than **M1**. This condition is consistent with our earlier DFT calculations. Moreover, the radial distribution functions (RDFs) among three individual chemical groups in the donor molecules (i.e., BDT, second thiophene unit of the terthiophene bridge (Th2), and RHD) and center-of-mass (COM) of C_{70} are analyzed for each system. RDF is the probability of finding other particles near around by drawing a series of circles about one certain particle. A diagrammatic sketch of RDF can be found in Figure S9. The results are shown in Figure 3d–f. In the case of the binary system, C_{70} is close to the BDT moieties in the **M1**:$PC_{71}BM$ system. In the case of the **M2**:$PC_{71}BM$ system, C_{70} is close to the bridge of Th2 due to the stronger steric effects of the longer side chains for the **M2** molecule. However, when 10% **M2** molecules are added to the **M1**:$PC_{71}BM$ binary blend, the RDF peak of RHD-C_{70} in the ternary system becomes the strongest.

DOI: 10.1021/jacs.7b13054
J. Am. Chem. Soc. 2018, 140, 1549−1556

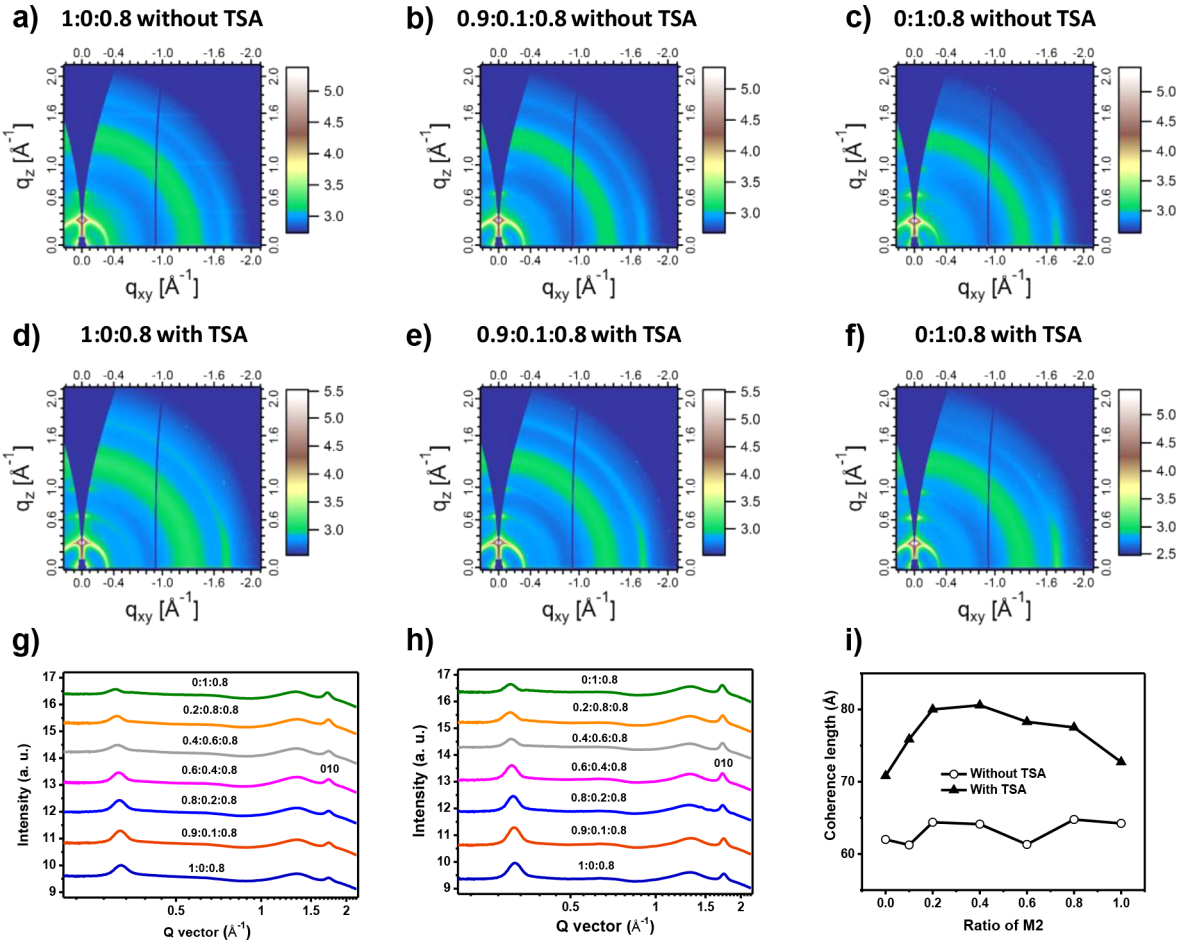

Figure 4. (a–c) 2D GIWAXS patterns of the active layers without TSA. (d–f) 2D GIWAXS patterns of the active layers with TSA. (g–h) 1D profiles along the in-plane direction without (g) and with (h) TSA. (i) Coherence length of (010) peaks that correspond to 1D profiles in (g) and (h).

This scenario implies that the probability of finding the $PC_{71}BM$ molecules close to the RHD moiety increased and results in the lesser extent of charge recombination. It is also consistent with recent experimental results by Graham et al. that pointed to the high efficiency of the polymer:fullerene system being obtained when the fullerene is generally docked with the electron-accepting moiety of the polymer.[37]

Morphology. The molecular stacking and orientation of the active layers was investigated by grazing incidence wide-angle X-ray scattering (GIWAXS).[38] Figure 4a–f presents the 2D GIWAXS patterns of selected binary and ternary blends. 2D GIWAXS patterns of other ternary systems are shown in Figure S10. In the in-plane direction, the $\pi-\pi$ stacking peaks (010) are located at q = 1.71–1.74 $Å^{-1}$, whereas the $\pi-\pi$ stacking peak is absent in the out-of-plane direction. The results indicate that the two π-conjugated small molecules and ternary blend have a preferred edge-on packing orientation with respect to the substrate. The corresponding in-plane cuts for all systems without and with TSA are shown in Figure 4g,h, respectively, to quantify the scattering data. The in-plane 1D profiles show that the (010) peaks of the **M1**:$PC_{71}BM$ and **M2**:$PC_{71}BM$ systems before TSA are located at q = 1.735 and 1.716 $Å^{-1}$, respectively, whereas the peaks after TSA are located at q = 1.742 and 1.720 $Å^{-1}$, respectively. The (010) locations of the ternary blends vary between the largest q of **M1** and smallest q of **M2** (Figure S11). The results indicate that **M2** has a larger $\pi-\pi$ stacking distance than **M1**. For all systems, the crystallinity is enhanced by TSA treatment because the coherence lengths of (010) peaks increase after TSA, which are shown in Figure 4i. The increased coherence length of the blends with an **M2** ratio of 10–20% can explain the enhancement in the FF of the corresponding devices. For the blends with an **M2** ratio of 40–80%, the device performance does not significantly change even with the larger coherence lengths. This scenario can be related to the large $\pi-\pi$ stacking distance. The (010) locations and coherence lengths were calculated by using the Scherrer analysis,[39] in which the full width at half-maximum were extracted by fitting the in-plane cuts with the Gaussian equation.

To deeply understand the morphological change introduced by TSA treatment, we performed the Gaussian fitting analysis for all (010) peaks of in-plane 1D cuts. According to the (010) peak locations of **M1** and **M2** in their binary blend films, we tried to divide the (010) peaks of ternary blend films into two peaks corresponding to **M1** and **M2**, respectively. As is shown in Figure S12, for data of films without TSA, it is quite difficult to obtain the distinguished two peaks, more precisely, the peaks that correspond to **M2**. When it comes to data of films with TSA, we can easily divide the (010) peaks into two fitting peaks correspond to **M1** and **M2** respectively (Figure S13), and the intensities of the fitted peaks are interestingly consistence with the **M1**:**M2** ratios in the ternary blend films. This could be an

DOI: 10.1021/jacs.7b13054
J. Am. Chem. Soc. 2018, 140, 1549–1556

evidence to the transformation from alloy-like model to cascade model for $\pi-\pi$ stacking is a significant factor of molecular assembly.

Trials were also made to do the same peak function fit analysis for the (100) peaks of 1D profiles because the (100) peaks directly reflect the molecular crystallization. However, due to the very similar chemical structures, the difference between the peak locations corresponding to **M1** and **M2** is negligible.

Therefore, another small molecule with longer BDT substitutional side chains, named C_6C_8-M1 (chemical structure is shown in Figure S14) was synthesized. Binary blend films and ternary blend films with C_6C_8-**M1**:**M2**:$PC_{71}BM$ ratio of 0.9:0.1:0.8 were made, and GIWAXS data were collected to analyze the influence introduced by TSA. The 2D patterns are shown in Figure S15, showing that after TSA treatment the crystallinity was enhanced, and more importantly, the (100) peak locations of 1D profiles along out-of-plane direction for ternary blend films show an obvious difference before and after TSA. As is shown in Figure S16, before TSA, the C_6C_8-M1:$PC_{71}BM$ film shows a (100) peak location of 0.29 $Å^{-1}$, **M2**:$PC_{71}BM$ film shows a (100) peak location of 0.34 $Å^{-1}$, and the ternary blend film gives a (100) peak location of 0.31 $Å^{-1}$. After TSA, both the C_6C_8-M1:$PC_{71}BM$ binary and the ternary blend film show (100) peak locations of around 0.30 $Å^{-1}$. This can be attributed to the fact that without TSA treatment C_6C_8-M1 and **M2** mix very well in the ternary blend films and the existence of small amount of **M2** influences the aggregation of C_6C_8-M1 causing a (100) peak shift. After TSA, **M2** shifts out from the mixed region to D−A interface showing little crystallization. Performance of devices based on C_6C_8-M1:$PC_{71}BM$ was also found to be enhanced after the inducement of 10% **M2** (as is shown in Table S4).

Transmission electron microscopy (TEM) was also performed to investigate the effect of morphological characteristics by adding **M2** to the host system. Figure S17 shows that the bright and dark regions in the TEM images correspond to the donors and $PC_{71}BM$-rich domains, respectively.[40,41] These images reveal that all systems show fibrous features with domain sizes of 15−20 nm, which benefit the exciton separation and charge transport.[42] The dark−bright contrast ratio of the **M1**:$PC_{71}BM$ and ternary blend images become higher after TSA, which imply a higher purity of domains introduced by annealing. As for the **M2**:$PC_{71}BM$ system, the domain size becomes slightly smaller after TSA.

Polymer:Small Molecule:Fullerene Solar Cells. To verify the effect of the interfacial optimization for ternary systems introduced by **M2**, another ternary solar cell based on the PTB7-Th:**M2**:$PC_{71}BM$ system is fabricated. With conventional device structures, the PTB7-Th:$PC_{71}BM$-based solar cells exhibit a PCE of 8.76% with a V_{OC} of 0.786 V, J_{SC} of 16.62 mA cm^{-2}, and FF of 67.5%. The PTB7-Th:**M2**:$PC_{71}BM$-based solar cells yield a high PCE of 9.44% with a V_{OC} of 0.786 V, J_{SC} of 16.77 mA cm^{-2}, and FF of 71.5%. A summary of the photovoltaic parameters of the solar cells based on PTB7-Th:**M2**:$PC_{71}BM$ is listed in Table S5. In the all-small-molecule ternary solar cells, a molecule that performs high interactions with $PC_{71}BM$ could serve as an interfacial sensitizer in polymer:small molecule:fullerene solar cells.

CONCLUSION

In conclusion, all-small-molecule ternary solar cells based on DR3TBDTT:DR3TBDTT-E: $PC_{71}BM$ have been designed and fabricated. In these cells, the new small molecule DR3TBDTT-E exhibits low HOMO and LUMO levels induced by ester-anchored side chains. A high PCE of 10.26% is achieved by the optimal ternary solar cells. It is believed that the ternary solar cells are correspond to an alloy-like model without thermal and solvent vapor annealing. However, a cascade model is formed after annealing because DR3TBDTT-E shifts from the mixed region to D−A interfaces and serves as a sensitizer, which is beneficial to charge separation process. PCE is also improved in the polymer:small molecule:fullerene ternary solar cells, and this finding indicates a universality of the interfacial optimizing function of DR3TBDTT-E. This transformation from an alloy-like level to a cascade level may provide useful information to fabricate high-performance OSCs.

ASSOCIATED CONTENT

Supporting Information

The Supporting Information is available free of charge on the ACS Publications website at DOI: 10.1021/jacs.7b13054.

Details for synthetic procedures, characterization of the materials, solar cells fabrication and measurement, fs-TAS measurements, DFT calculations, MD simulations, GIWAXS and TEM characterizations (PDF)

AUTHOR INFORMATION

Corresponding Authors

*E-mail: lvk@nanoctr.cn.
*E-mail: zhuly@nanoctr.cn.
*E-mail: msewma@xjtu.edu.cn.
*E-mail: weizx@nanoctr.cn.

ORCID

Wei Ma: 0000-0002-7239-2010
Zhigang Shuai: 0000-0003-3867-2331
Zhixiang Wei: 0000-0001-6188-3634

Author Contributions

Zhen Wang and Xiangwei Zhu contributed equally.

Notes

The authors declare no competing financial interest.

ACKNOWLEDGMENTS

We acknowledge the financial support from the Ministry of Science and Technology of China (Grant No. 2016YFA0200700), the National Natural Science Foundation of China (Grant Nos. 21474022, 21473043, 21773040, 51773047, 51673049, and 21604017) and the "Strategic Priority Research Program" of the Chinese Academy of Sciences (Grant No. XDA0909040201). MD simulations were carried out on TianHe-1 (A) at the National Supercomputer Center in Tianjin, China. X-ray data were acquired at beamlines 7.3.3 at the Advanced Light Source, which is supported by the Director, Office of Science, Office of Basic Energy Sciences, of the U.S. Department of Energy under Contract No. DE-AC02-05CH11231. The fs-TAS measurements were conducted with the help of Prof. Xinfeng Liu and Dr. Yang Mi at the National Center for Nanoscience and Technology, China.

REFERENCES

(1) Dou, L.; You, J.; Hong, Z.; Xu, Z.; Li, G.; Street, R. A.; Yang, Y. *Adv. Mater.* **2013**, *25*, 6642.

DOI: 10.1021/jacs.7b13054
J. Am. Chem. Soc. 2018, 140, 1549−1556

(2) Krebs, F. C.; Espinosa, N.; Hösel, M.; Søndergaard, R. R.; Jørgensen, M. *Adv. Mater.* **2014**, *26*, 29.
(3) Lu, L.; Zheng, T.; Wu, Q.; Schneider, A. M.; Zhao, D.; Yu, L. *Chem. Rev.* **2015**, *115*, 12666.
(4) Zhao, W.; Li, S.; Yao, H.; Zhang, S.; Zhang, Y.; Yang, B.; Hou, J. *J. Am. Chem. Soc.* **2017**, *139*, 7148.
(5) Deng, D.; Zhang, Y.; Zhang, J.; Wang, Z.; Zhu, L.; Fang, J.; Xia, B.; Wang, Z.; Lu, K.; Ma, W.; Wei, Z. *Nat. Commun.* **2016**, *7*, 13740.
(6) Ameri, T.; Khoram, P.; Min, J.; Brabec, C. J. *Adv. Mater.* **2013**, *25*, 4245.
(7) Cheng, P.; Zhan, X. *Mater. Horiz.* **2015**, *2*, 462.
(8) Li, H.; Lu, K.; Wei, Z. *Adv. Energy Mater.* **2017**, *7*, 1602540.
(9) Yang, L.; Zhou, H.; Price, S. C.; You, W. *J. Am. Chem. Soc.* **2012**, *134*, 5432.
(10) Khlyabich, P. P.; Burkhart, B.; Thompson, B. C. *J. Am. Chem. Soc.* **2011**, *133*, 14534.
(11) Khlyabich, P. P.; Burkhart, B.; Thompson, B. C. *J. Am. Chem. Soc.* **2012**, *134*, 9074.
(12) Street, R. A.; Davies, D.; Khlyabich, P. P.; Burkhart, B.; Thompson, B. C. *J. Am. Chem. Soc.* **2013**, *135*, 986.
(13) Khlyabich, P. P.; Rudenko, A. E.; Thompson, B. C.; Loo, Y.-L. *Adv. Funct. Mater.* **2015**, *25*, 5557.
(14) Yang, Y.; Chen, W.; Dou, L.; Chang, W.-H.; Duan, H.-S.; Bob, B.; Li, G.; Yang, Y. *Nat. Photonics* **2015**, *9*, 190.
(15) Zhang, Y.; Deng, D.; Lu, K.; Zhang, J.; Xia, B.; Zhao, Y.; Fang, J.; Wei, Z. *Adv. Mater.* **2015**, *27*, 1071.
(16) Zhang, J.; Zhang, Y.; Fang, J.; Lu, K.; Wang, Z.; Ma, W.; Wei, Z. *J. Am. Chem. Soc.* **2015**, *137*, 8176.
(17) Lu, L.; Kelly, M. A.; You, W.; Yu, L. *Nat. Photonics* **2015**, *9*, 491.
(18) An, Q.; Zhang, F.; Zhang, J.; Tang, W.; Deng, Z.; Hu, B. *Energy Environ. Sci.* **2016**, *9*, 281.
(19) Bartelt, J. A.; Beiley, Z. M.; Hoke, E. T.; Mateker, W. R.; Douglas, J. D.; Collins, B. A.; Tumbleston, J. R.; Graham, K. R.; Amassian, A.; Ade, H.; Fréchet, J. M. J.; Toney, M. F.; McGehee, M. D. *Adv. Energy Mater.* **2013**, *3*, 364.
(20) Burke, T. M.; McGehee, M. D. *Adv. Mater.* **2014**, *26*, 1923.
(21) Scarongella, M.; De Jonghe-Risse, J.; Buchaca-Domingo, E.; Causa', M.; Fei, Z.; Heeney, M.; Moser, J.-E.; Stingelin, N.; Banerji, N. *J. Am. Chem. Soc.* **2015**, *137*, 2908.
(22) Xu, H.; Ohkita, H.; Tamai, Y.; Benten, H.; Ito, S. *Adv. Mater.* **2015**, *27*, 5868.
(23) Nian, L.; Gao, K.; Liu, F.; Kan, Y.; Jiang, X.; Liu, L.; Xie, Z.; Peng, X.; Russell, T. P.; Ma, Y. *Adv. Mater.* **2016**, *28*, 8184.
(24) Peet, J.; Tamayo, A. B.; Dang, X. D.; Seo, J. H.; Nguyen, T. Q. *Appl. Phys. Lett.* **2008**, *93*, 163306.
(25) Honda, S.; Nogami, T.; Ohkita, H.; Benten, H.; Ito, S. *ACS Appl. Mater. Interfaces* **2009**, *1*, 804.
(26) Huang, J.-H.; Velusamy, M.; Ho, K.-C.; Lin, J.-T.; Chu, C.-W. *J. Mater. Chem.* **2010**, *20*, 2820.
(27) Koppe, M.; Egelhaaf, H.-J.; Dennler, G.; Scharber, M. C.; Brabec, C. J.; Schilinsky, P.; Hoth, C. N. *Adv. Funct. Mater.* **2010**, *20*, 338.
(28) Honda, S.; Ohkita, H.; Benten, H.; Ito, S. *Adv. Energy Mater.* **2011**, *1*, 588.
(29) Honda, S.; Yokoya, S.; Ohkita, H.; Benten, H.; Ito, S. *J. Phys. Chem. C* **2011**, *115*, 11306.
(30) Gasparini, N.; Salvador, M.; Fladischer, S.; Katsouras, A.; Avgeropoulos, A.; Spiecker, E.; Chochos, C. L.; Brabec, C. J.; Ameri, T. *Adv. Energy Mater.* **2015**, *5*, 1501527.
(31) Gasparini, N.; Jiao, X.; Heumueller, T.; Baran, D.; Matt, G. J.; Fladischer, S.; Spiecker, E.; Ade, H.; Brabec, C. J.; Ameri, T. *Nat. Energy* **2016**, *1*, 16118.
(32) Zhou, J.; Zuo, Y.; Wan, X.; Long, G.; Zhang, Q.; Ni, W.; Liu, Y.; Li, Z.; He, G.; Li, C.; Kan, B.; Li, M.; Chen, Y. *J. Am. Chem. Soc.* **2013**, *135*, 8484.
(33) Riedel, I.; Parisi, J.; Dyakonov, V.; Lutsen, L.; Vanderzande, D.; Hummelen, J. C. *Adv. Funct. Mater.* **2004**, *14*, 38.
(34) Cowan, S. R.; Roy, A.; Heeger, A. J. *Phys. Rev. B: Condens. Matter Mater. Phys.* **2010**, *82*, 245207.
(35) Lu, L.; Chen, W.; Xu, T.; Yu, L. *Nat. Commun.* **2015**, *6*, 7327.
(36) Hess, B.; Kutzner, C.; van der Spoel, D.; Lindahl, E. *J. Chem. Theory Comput.* **2008**, *4*, 435.
(37) Graham, K. R.; Cabanetos, C.; Jahnke, J. P.; Idso, M. N.; El Labban, A.; Ngongang Ndjawa, G. O.; Heumueller, T.; Vandewal, K.; Salleo, A.; Chmelka, B. F.; Amassian, A.; Beaujuge, P. M.; McGehee, M. D. *J. Am. Chem. Soc.* **2014**, *136*, 9608.
(38) Muller-Buschbaum, P. *Adv. Mater.* **2014**, *26*, 7692.
(39) Smilgies, D.-M. *J. Appl. Crystallogr.* **2009**, *42*, 1030.
(40) Ma, W.; Kim, J. Y.; Lee, K.; Heeger, A. J. *Macromol. Rapid Commun.* **2007**, *28*, 1776.
(41) Su, M.-S.; Kuo, C.-Y.; Yuan, M.-C.; Jeng, U. S.; Su, C.-J.; Wei, K.-H. *Adv. Mater.* **2011**, *23*, 3315.
(42) Chen, H.-Y.; Hou, J.; Zhang, S.; Liang, Y.; Yang, G.; Yang, Y.; Yu, L.; Wu, Y.; Li, G. *Nat. Photonics* **2009**, *3*, 649.

DOI: 10.1021/jacs.7b13054
J. Am. Chem. Soc. 2018, 140, 1549−1556